Improving the Precision of Near-Infrared Stellar Photometry by Modeling the Image Formation Process within a Lossy Detector

Kenneth Mighell
National Optical Astronomy Observatory
950 North Cherry Avenue
Tucson, AZ 85719 U.S.A.

***Abstract*—A detector can be considered to be effectively lossy if a pixel, the smallest optically sensitive unit of the detector, internally exhibits a non-uniform response function that has a quantum efficiency variation with an rms dispersion exceeding an arbitrary level of 1%. Near-infrared astronomical cameras based on lossy detectors can have large systematic errors in the measurement of total stellar flux if stellar images are undersampled. While this problem can be mitigated by oversampling the stellar image, many near-infrared cameras are deliberately undersampled in order to achieve a large field of view. The combination of undersampling stellar images on lossy detectors is currently diminishing the potential science return of some of the near-infrared cameras onboard the *Hubble Space Telescope* and the *Spitzer Space Telescope*. Although the recorded stellar flux can be corrupted by using detectors with significant effective intrapixel quantum efficiency variations, it is still possible to achieve excellent stellar photometry – if the image formation process inside the detector is accurately modeled. During the past year, I have worked with *Spitzer Space Telescope*'s Infrared Array Camera (IRAC) Instrument Team to demonstrate that my NASA-funded MATPHOT algorithm for precision stellar photometry and astrometry using discrete Point Spread Functions can yield an improvement in the precision of bright star stellar photometry, obtained from IRAC Ch1 observations, of more than 100% over the best results obtained with aperture photometry using the recommended calibration procedures in the IRAC Data Handbook. This collaborative effort will continue with the goal of developing new calibration procedures for that have the potential of significantly improving the precision of IRAC point-source photometry. This effort is timely because IRAC Ch1 and Ch2 will be the only operational cameras available during the Spitzer Warm Mission which is nominally scheduled to start about April 2009 after all of the cryogen has been depleted. This work was supported by grants from the Applied Information Systems Research (AISR) Program of NASA's Science Mission Directorate.**

I. Introduction

Current near-infrared detector technology can produce space-based astronomical imagers with non-uniform pixel response functions. Large intrapixel quantum efficiency (QE) variations can cause significant loss of stellar flux depending on where a star is centered within the central pixel of the stellar image. Reference [1] measured a peak-to-peak variation of 0.39 mag at the J band (F110W) and 0.22 mag at H band (F160W) of the NIC3 camera of the *Hubble Space Telescope* (*HST*) NICMOS instrument [2], [3]. The peak-to-peak variation of $\sim$0.2 mag at F160W with NIC3 has been independently verified [4]. Significant flux loss due to non-uniform intrapixel response functions is clearly an observational fact in some existing space-based near-infrared astronomical cameras.

Even existing NASA-grade optical CCDs (charge coupled devices) can have minor intrapixel QE variations across a single pixel. Reference [1] found that the V-band (F555W) Point Spread Function (PSF) of the WFC (Wide Field Camera) of the *HST* WFPC2 instrument [5], [6] has a peak-to-peak range of 0.030 mag and an rms dispersion of 0.008 mag; the effect at the I band (F814W) is slightly better with a peak-to-peak error range of 0.023 mag with a 0.006 mag dispersion. This small but measurable variation of the quantum efficiency within a WFC pixel is a contributing factor to the minimum image-to-image photometric scatter of 0.01 mag that has been found in dithered WFPC2 stellar observations (see, e.g., [7]–[12]).

NASA (National Aeronautics and Space Administration) and ESA (European Space Agency) astrophysical mission managers have a penchant for approving of camera designs which use undersampled detectors on the focal plane in order to achieve a wider field of view. Unfortunately, the analysis of image data from cameras with undersampled detectors is frequently problematical. Analysis difficulties are further compounded when the detectors used in such cameras are lossy.

A detector can be considered to be effectively lossy if a pixel, the smallest optically sensitive unit of the detector, internally exhibits a non-uniform response function that has a quantum efficiency variation with an rms dispersion exceeding an arbitrary level of 1%. By this user-centric definition, the detectors in NIC3 camera of the NICMOS instrument are lossy but the detectors used in the WFC cameras of the WFPC2 instrument are not.

This article describes how the precision of stellar photometry from an existing space-based near-infrared camera with a lossy detector can be significantly improved by compensating the apparent loss of stellar flux through modeling of the image formation process within the detector. Section II describes the role of Point Response Functions in the image formation process. A photometric and astrometric perfomance model for CCD stellar observations is given in Section III. The key features of the MATPHOT algorithm for precision stellar pho-

tometry and astrometry with discrete (sampled) Point Spread Functions are briefly outlined in Section IV. Observations of a bright star obtained with Channel 1 of the *Spitzer Space Telescope* Infrared Array Camera (IRAC) instrument are described in Section V and analyzed using aperture photometry in Section VI and then MATPHOT photometry in Section VII. Concluding remarks are given in Section VIII.

II. Point Response Functions

A Point Response Function (PRF), Ψ, of an astronomical imaging system with a detector is the convolution of a Point Spread Function (PSF), ϕ, and a Detector Response Function (DRF), Λ :

$$\Psi \equiv \phi * \Lambda \ . \tag{1}$$

The PSF describes the two-dimensional distribution of photons from a star *just above the detector.* Although stellar photons are distributed as a point source above the Earth's atmosphere, a stellar image becomes a two-dimensional distribution as the stellar photons are scattered by atmospheric turbulence. The blurred stellar image is then further degraded by passage of the stellar photons through the combined telescope and camera optical elements (such as mirrors, lenses, apertures, etc.). The PSF is the convolution of all these blurring effects on the original stellar point source.

The DRF is a two-dimensional discrete (sampled) function that describes how the detector electronics convert stellar photons (γ) to electrons (e^-) — including such effects as the diffusion of electrons within the detector substrate or the reflection (absorption) of photons on (in) the gate structures of the detector electronics. A perfect DRF gives a PRF that is a *sampled version* of the PSF:

$$\Psi_i \equiv \int_{x_i-0.5}^{x_i+0.5} \int_{y_i-0.5}^{y_i+0.5} \phi(x,y)\, dx\, dy \ , \tag{2}$$

where $i^{\rm th}$ pixel (px) of the PRF located at (x_i, y_i) is the volume integral of the PSF over the area of the $i^{\rm th}$ pixel. The actual limits of the above volume integral reflect the appropriate mapping transformation of the x and y coordinates onto the CCD pixel coordinate system.

The volume, V, of a PRF is, by definition, one or less:

$$\mathrm{V} \equiv \iint (\phi * \Lambda)\ dx\, dy \equiv \sum_i \Psi_i \quad \leq \quad 1 \ , \tag{3}$$

where the integration and summation are over all pixels which are illuminated by the PSF. A PRF volume that is less than one indicates that a loss of stellar photons has occurred during the detection/conversion process within the detector.

The effective-background area, $\boldsymbol{\beta}$, of a PRF is defined as the reciprocal of the summation of the square of the PRF:

$$\boldsymbol{\beta} \equiv \frac{1}{\sum_i \Psi_i^2} \, . \tag{4}$$

Physically, $\boldsymbol{\beta}$ can be thought of as the noise "footprint" (in pixels) of a stellar image on the sky. The effective-background area is an observing-efficiency metric (small $\boldsymbol{\beta}$ values are better) that is used to make accurate predictions of the photometric and astrometric performance limits of stellar observations obtained with state-of-the-art astrophysical imagers with lossy detectors; this metric measures the combination of camera focus and detector efficiency: for any given detector, the smallest $\boldsymbol{\beta}$ values are obtained when the camera is focused and, similarly, for any given focus, the smallest $\boldsymbol{\beta}$ values are obtained when the efficiency of the detector is maximized [13].

The S_1 image sharpness parameter from the seminal paper of Muller & Buffington [14] is the summation of the square of the normalized PRF:

$$\mathsf{S}_1 \equiv \sum_i \tilde{\Psi}_i^2 \equiv \sum_i \left(\frac{\Psi_i}{V} \right)^2 \equiv \mathsf{sharpness} \, . \tag{5}$$

Physically, S_1 is a shape parameter that describes the "pointiness" of a PRF; S_1 values range from a maximum of one (all of the stellar flux is found within a single pixel) to a minimum of zero (a flat stellar image). For example, cameras that are out of focus have broad PSFs with S_1 values near zero. A normalized Gaussian [15] PSF with a standard deviation of $\boldsymbol{\sigma}$ pixels that has been *oversampled* with a perfect DRF (where $\mathrm{V} = 1$) will have a S_1 value of $1/4\pi\boldsymbol{\sigma}^2$. A *critically-sampled* normalized Gaussian PRF (where $\boldsymbol{\sigma} \equiv 1$) thus has a S_1 value of $1/(4\pi)$ and any PRF with a S_1 value greater than that value (~ 0.0796) can be described as being undersampled. The S_1 image sharpness parameter has proven to be such a useful image quality metric that one finds references to it in the astrophysical literature where it is simply called sharpness without citing Muller & Buffington (see, e.g., Section 6.5.1 of [6] and Section 2.1 of [13]).

Diffraction limited optics, theoretically, give S_1 values that decrease (i.e., PSFs become flatter) with increasing photon wavelength – for a fixed pixel (detector) size. With real astronomical cameras, observed S_1 values frequently depend on *where the center of a star is located within the central CCD pixel* of the stellar image. For example, the *HST* WFPC2 Planetary Camera PRF at a wavelength of 200 nm has an observed S_1 value of 0.084 if the PRF is centered in the middle of a PC pixel or 0.063 if the PRF is centered on a pixel corner (see Table 6.5 of [6]); at 600 nm the observed S_1 values range from 0.066 (pixel-centered) to 0.054 (corner-centered). The Wide-Field Cameras of the *HST* WFPC2 instrument have pixels which are approximately half the angular resolution of the PC camera pixels; WFC stellar images are undersampled and the observed range of S_1 values are 0.102–0.120 at 200 nm and 0.098–0.128 at 600 nm.

The *normalized* effective-background area, $\tilde{\boldsymbol{\beta}}$, of a PRF is defined as the reciprocal of the summation of the square of the normalized PRF; it is a focus metric which has an optimal (minimum) value when a camera is in focus. The normalized effective-background area of a PRF, also called NoisePixels by the IRAC Instrument Team (see, e.g., [16]–[19]), is equivalent

to the inverse of the S_1 image sharpness parameter:

$$\tilde{\boldsymbol{\beta}} \equiv \frac{1}{\sum_i \tilde{\Psi}_i^2} \equiv \boldsymbol{\beta}\,\mathrm{V}^2 \equiv \frac{1}{\mathsf{S}_1} \equiv \mathsf{NoisePixels}\,. \tag{6}$$

A critically-sampled Gaussian PSF has a normalized effective-background area value of 4π ($\approx$12.57) px; any PRF can be considered to be undersampled if $\tilde{\boldsymbol{\beta}} < 4\pi$. Numerical integration of a realistic ground-based stellar profile gives a normalized effective-background area of $30.8\,\boldsymbol{\sigma}^2$ instead of the value of $4\pi\,\boldsymbol{\sigma}^2$ for a Gaussian profile with a standard deviation of $\boldsymbol{\sigma}$ pixels [20].

III. Performance Model

Consider a CCD observation of single isolated star on a flat sky background. Assuming one already knows the PRF of the observation at the location of the star, a simple model of the observation would have just two parameters: the stellar intensity ($\mathcal{E}$) in electrons, and the observed background sky level ($\mathcal{B}$) in electrons. The observational model for the i^{th} pixel would be

$$m_i \equiv \mathcal{B} + \mathcal{E}\mathrm{V}\tilde{\Psi}_i\ , \tag{7}$$

where V is the volume integral of the PRF and $\tilde{\Psi}_i$ is the value of the i^{th} pixel of the *normalized* PRF ($\tilde{\Psi}_i \equiv \Psi_i/\mathrm{V}$).

The *upper limit* for the photometric signal-to-noise ratio ($\mathsf{S/N}$) of a CCD observation of a single isolated star on a flat sky can be estimated as follows:

$$\begin{aligned}
\mathsf{S/N} &\equiv \frac{\mathcal{E}}{\sigma_{\mathcal{E}}} \\
&\approx \frac{\mathcal{E}}{\sqrt{\dfrac{\mathcal{E}}{\mathrm{V}} + \boldsymbol{\beta}\left(1+\sqrt{\boldsymbol{\beta}/N}\right)^2 \sigma_{\mathrm{rms}}^2}} &(8)\\
&\approx \frac{\mathcal{E}}{\sqrt{\dfrac{\mathcal{E}}{\mathrm{V}} + \boldsymbol{\beta}\left(1+\sqrt{\boldsymbol{\beta}/N}\right)^2 \left[\mathcal{B}+\sigma_{\mathrm{RON}}^2\right]}} &(9)
\end{aligned}$$

where

$$\sigma_{\mathrm{rms}} \equiv \sqrt{\frac{1}{N}\sum_{i=1}^{N}\sigma_i^2} \approx \sqrt{\mathcal{B}+\sigma_{\mathrm{RON}}^2}\ , \tag{10}$$

N is the number of pixels in the observation, σ_i is the measurement error (one standard deviation) of the i^{th} pixel, the background sky is assumed to be a Poisson distribution with a mean of $\mathcal{B}$ electrons, and σ_{RON} is the rms readout noise [13]. These approximations assume, for the sake of simplicity, that any noise contribution due to dark current and quantization noise is negligible. While these additional noise sources can be added to create an even more realistic performance model for stellar photometry, the assumption of low dark current and minimal quantization noise is realistic for state-of-the-art astronomical-grade CCD imagers. The resulting photometric error is approximately

$$\Delta\mathsf{mag} \approx \frac{1.0857}{\mathsf{S/N}}\ , \tag{11}$$

where the constant 1.0857 is an approximation for Pogson's ratio $a \equiv 5/\ln(100) = 2.5\log(e)$ [21].

The *lower limit* of the rms measurement error for the stellar $\mathcal{X}$ position of a CCD observation of a single isolated star on a flat sky can be estimated as follows:

$$\begin{aligned}
\sigma_{\mathcal{X}} &\approx \sqrt{\frac{\mathcal{L}^2}{\mathcal{E}\mathrm{V}}\left[1+8\pi\,\sigma_{\mathrm{rms}}^2\frac{\mathcal{L}^2}{\mathcal{E}\mathrm{V}}\right]} &(12)\\
&\approx \sqrt{\frac{\mathcal{L}^2}{\mathcal{E}\mathrm{V}}\left[1+8\pi\left(\mathcal{B}+\sigma_{\mathrm{RON}}^2\right)\frac{\mathcal{L}^2}{\mathcal{E}\mathrm{V}}\right]} &(13)
\end{aligned}$$

where

$$\mathcal{L} \equiv \sqrt{\frac{\tilde{\boldsymbol{\beta}}}{4\pi}} = \frac{1}{\sqrt{4\pi\,\mathsf{S}_1}} \tag{14}$$

is the *critical-sampling scale length* of the PRF in pixel units (px) [13]. By definition, the critical-sampling scale length of a critically-sampled PRF imaged with a perfect detector is one pixel; $\mathcal{L} > 1$ indicates that the PRF is *oversampled*, while $\mathcal{L} < 1$ indicates that the PRF is *undersampled*.

The *lower limit* of the rms measurement error for the stellar $\mathcal{Y}$ position of a CCD observation of a single isolated star on a flat sky can be estimated, by symmetry, as follows:

$$\sigma_{\mathcal{Y}} = \sigma_{\mathcal{X}}\ . \tag{15}$$

IV. MATPHOT Algorithm

The MATPHOT algorithm for precise and accurate stellar photometry and astrometry with discrete PSFs was described in detail in reference [13]. The current C-language [22] implementation of the MATPHOT algorithm works with user-provided discrete (sampled) PSFs consisting of a numerical table represented by a matrix in the form of a FITS image [23]. Position partial derivatives are computed [24] using the following five-point numerical differentiation formula,

$$\begin{aligned}
&f'(x_i)\\
&\quad\approx \frac{1}{12}\left[f(x_{i-2}) - 8\,f(x_{i-1}) + 8\,f(x_{i+1}) - f(x_{i+2})\right]\ , &(16)
\end{aligned}$$

from [25], and discrete PSFs are shifted [26] within an observational model using the following 21-pixel-wide damped sinc function,

$$\begin{aligned}
&f^{\mathrm{shifted}}(x_0)\\
&\quad\equiv \sum_{i=-10}^{10} f(x_i)\frac{\sin\left(\pi(x_i-x_0)\right)}{\pi(x_i-x_0)}\exp\left(-\left[\frac{x_i-x_0}{3.25}\right]^2\right), &(17)
\end{aligned}$$

from the ZODIAC C library written by Marc Buie of Lowell Observatory, which was specifically designed for use with 32-bit floating numbers. Precise and accurate stellar photometry and astrometry are achieved with undersampled CCD observations by using supersampled discrete PSFs that are sampled 2, 3, or more times more finely than the observational data. Although these numerical techniques are not mathematically

perfect, they are sufficiently accurate for precision stellar photometry and astrometry due to photon noise which is present in all astronomical imaging observations. The current photometric reduction code[1] is based on a robust implementation of the Levenberg-Marquardt method of nonlinear least-squares minimization [27]–[30]. Detailed analysis of simulated *Next Generation Space Telescope* (*NGST*) observations demonstrate that millipixel relative astrometry and millimag photometric precision should be achievable with complicated space-based discrete PSFs [13]. The MATPHOT algorithm achieves the theoretical performance expectations [13] for accurate and precise stellar photometry and astrometry described in the previous section.

V. Observations

I analyzed 16 short (0.6 s) frames[2] from a focus check calibration on the K0-class star PPM 9412 (a.k.a. HIP 6378) from Channel 1 (3.6 μm) of the Infrared Array Camera (IRAC) [19] onboard the *Spitzer Space Telescope*. The observation was on 2003 October 8 UT, after all focus adjustments had been completed. The locations of the star on the array were distributed roughly evenly across a 4x4 pixel box near the array center. The IRAC basic calibrated data (BCD) images were retrieved from the *Spitzer* data archive with the kind assistance of IRAC Instrument Team member Bill Glaccum.

VI. Aperture Photometry

Square aperture photometry with a 21×21 pixel box centered on a star was performed using the interactive "m" keyboard command of the *imexamine* task of the IRAF data reduction and analysis system [31], [32]. A 5.6% peak-to-peak spread was seen in these square aperture flux measurements (see Fig. 1). *A nonrandom variation in flux is quite apparent in these 16 IRAC Ch1 observations:* the total stellar flux measured is strongly correlated with the amount of flux found in the central pixel (see Fig. 2).

Examination of the individual observations revealed that the observations with the most stellar flux have stellar images that are centered in the middle of a pixel while those observations with the least stellar flux are centered on a pixel corner. This effect, shown graphically in Fig. 3 (which is Fig. 5.1 of the IRAC Data Handbook [33]), is due to the combination of large quantum efficiency variations within individual pixels and the undersampling of the Point Spread Function (PSF) by the Detector Response Function (DRF). The loss flux is most severe in Channel 1 (3.6 μm) where the correction can be as much as 4% peak to peak [33].

[1]All source code and documentation for MATPHOT and support software are freely available at NOAO: http://www.noao.edu/staff/mighell/matphot

[2]Observations: ads/sa.spitzer#00068nnnnn where nnnnn is 75392, 76672, 76928, 77184, 77440, 77696, 77952, 78208, 78464, 78720, 78976, 79232, 79488, 79744, 80000, 80256.

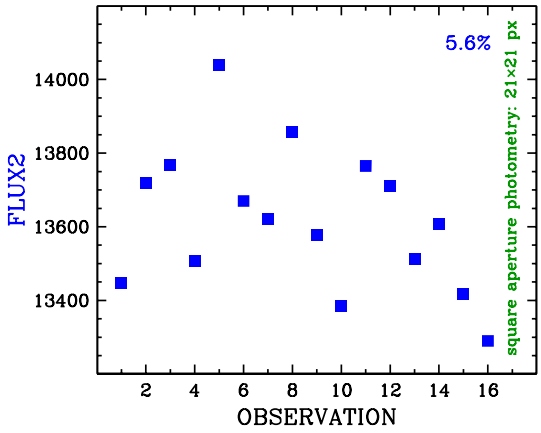

Fig. 1. Square aperture photometry of IRAC Ch1 observations of a single bright star.

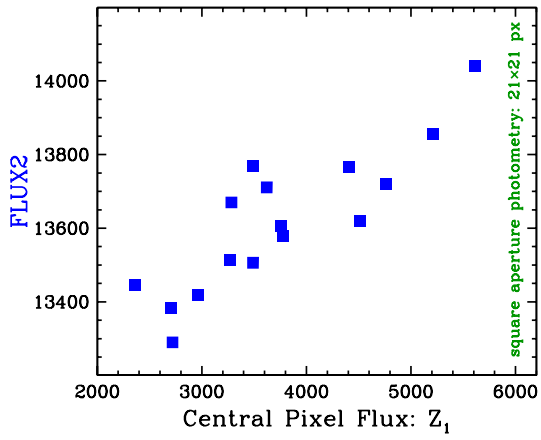

Fig. 2. Same data as in Fig. 1 but sorted by the flux value of the central pixel of the stellar image.

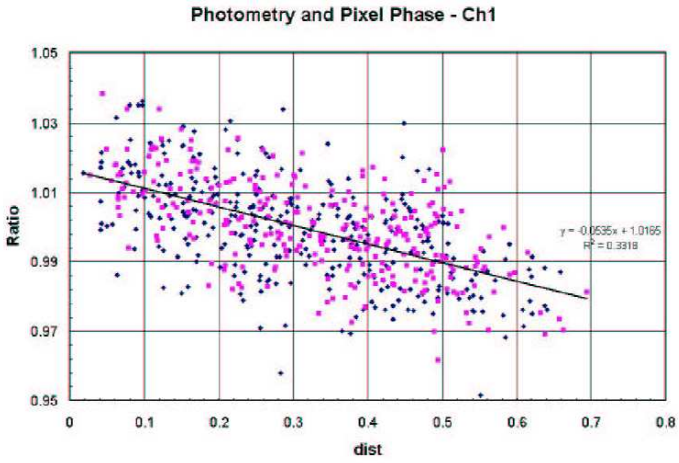

Fig. 3. **Figure 5.1 of the IRAC Data Handbook** [33]. Dependence of point source photometry on the distance of the centroid of a point source from the nearest pixel center in channel 1. The ratio on the vertical axis is the measured flux density to the mean value for the star, and the quantity on the horizontal axis is the fractional distance of the centroid from the nearest pixel center.

This is the relevant extract from the IRAC Data Handbook [33]:

> The flux density of a point source measured from IRAC images depends on the exact location where the peak of the Point Response Function (PRF) falls on a pixel. This effect is due to the variations in the quantum efficiency of a pixel, and combined with the undersampling of the PRF, it is most severe in channel 1. The correction can be as much as 4% peak to peak. The effect is graphically shown in Figure 5.1 *(see Fig. 3 of this article)* where the normalized measured flux density (y-axis) is plotted against the distance of the source centroid from the center of a pixel. The correction for channel 1 can be calculated from
>
> $$Correction = 1 + 0.0535 \times \left[\frac{1}{\sqrt{2\pi}} - p \right] \qquad (5.14)$$
>
> where p is the pixel phase ($p = \sqrt{(x-x_0)^2+(y-y_0)^2}$), where x, y, is the centroid of the point source and x_0 and y_0 are the integer pixel numbers containing the source centroid. The correction was derived from photometry of a sample of stars, each star observed at many positions on the array. The "ratio" on the vertical axis in Figure 5.1 is the ratio of the measured flux density to the mean value for the star. To correct the flux of a point source, calculate the correction from Equation 5.14 and divide the source flux by that correction. Thus, the flux of sources well-centered in a pixel will be reduced by 2.1%. Pixel phase corrections for other channels, if necessary, and after they have been more accurately determined than currently, will be given in future Data Handbook versions.

The application of the recommended radial flux correction requires an accurate estimate of the position of the center of the star. IRAF's *imexamine* task can produce accurate centroid estimates for circular aperture photometry but not for square aperture photometry. So in order to apply the radial flux correction recommended by the IRAC Data Handbook, circular aperture photometry was performed on the observations shown in Fig. 1.

Circular aperture photometry centered on the star with a radius of 10 pixels (px) was done using the interactive "a" keyboard command of the *imexamine* task of IRAF. A **5.3%** peak-to-peak spread was found in the raw circular aperture flux measurements (see Fig. 4: open circles). Applying the recommended Ch1 flux correction from the IRAC Data Handbook only slightly reduced the peak-to-peak spread to **4.9%** (see Fig. 4: filled circles) .

Reducing the aperture radius to just 5 pixels does improve the photometric precision; a **4.5%** peak-to-peak spread was found in the raw circular aperture flux measurements (see Fig. 5: open circles) which reduced to **3.5%** when the recommended Ch1 flux correction was applied (see Fig. 5: filled circles). *This is the best that aperture photometry can do with the recommended radial correction.*

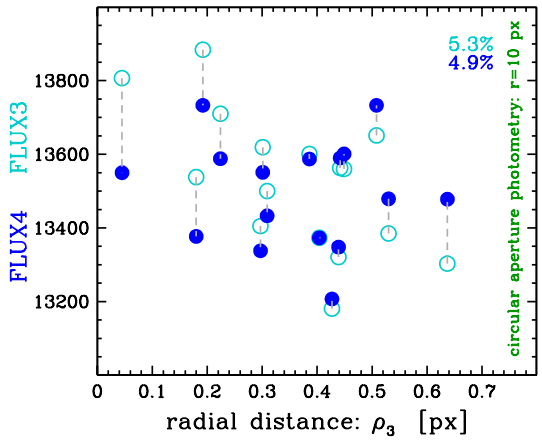

Fig. 4. Circular aperture photometry with a radius of 10 pixels of the observations shown in Fig. 1. The filled (open) circles show the corrected (raw) flux values.

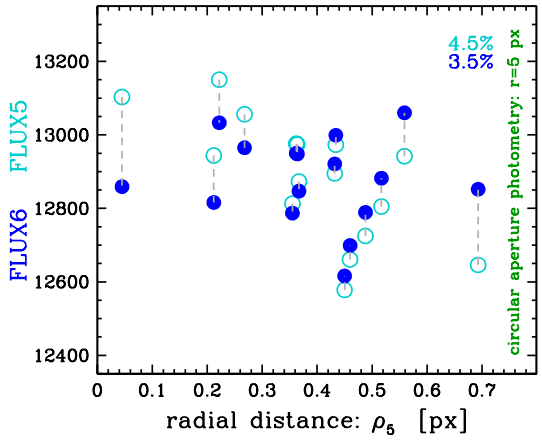

Fig. 5. Circular aperture photometry with a radius of 5 pixels. The filled (open) circles show the corrected (raw) flux values.

VII. MATPHOT PHOTOMETRY

IRAC Ch1 PSFs are significantly undersampled by the IRAC Ch1 camera [19]. A theoretical 5×5 supersampled version of the IRAC PSF for the central region of Ch1 is shown in Fig. 6 [34]. Although the PSF appears to be reasonable in the linear stretch *(left graph)*, which emphasizes the bright central core, the log stretch *(right graph)* shows the numerous weak higher-spatial-frequency features of this very complicated PSF.

Bill Hoffmann, an IRAC Instrument Team member at the University of Arizona, made the first estimate [35] of the intrapixel quantum efficiency variation across a single IRAC Ch1 pixel:

$$\text{intrapix} = \begin{pmatrix} 0.813 & 0.875 & 0.875 & 0.875 & 0.813 \\ 0.875 & 1.000 & 1.000 & 1.000 & 0.875 \\ 0.875 & 1.000 & 1.000 & 1.000 & 0.875 \\ 0.875 & 1.000 & 1.000 & 1.000 & 0.875 \\ 0.813 & 0.875 & 0.875 & 0.875 & 0.813 \end{pmatrix} .$$

Each element is the mean RQE (relative quantum efficiency) value, *relative to the center of the pixel*, over a 0.2×0.2 pixel^2

area. Such a variation in QE across a pixel could be obtained if photogenerated charges originating at a pixel edge are more likely to recombine than charges originating near a pixel center, because they must random walk further before being collected. The QE variation is expected to be symmetrical about the center of a pixel, since the InSb layer is opaque over the bandpasses of Channels 1 and 2.

An experimental version of the MATPHOT stellar photometry code, called MPDZ, was developed to simulate and analyze IRAC Ch1 observations [36]–[39]. MPDZ models the image formation process within IRAC Ch1 by convolving the 5×5 supersampled theoretical PSF for the central region of IRAC Ch1 PSF shown in Fig. 6 with the above relative intrapixel quantum efficiency (QE) variation map for IRAC Ch1.

Ten thousand IRAC Ch1 observations of a single star on a flat background were simulated and analyzed with MPDZ. Each stellar observation was simulated using the PSF shown above; a star with an intensity of 10^6 electrons was located near the center of an field of 60×60 pixels on a flat background of 100 electrons.

The horizontal axis of Fig. 7 shows the subpixel offset (radial distance) the center of a star is from the middle of the central pixel; stars centered near the middle of a pixel will have small offset values while stars located near the corner of a pixel will have offsets near 0.7 px. The vertical axis of Fig. 7 shows the absolute flux ratio of the total fluxes divided by the true flux of 10^6 electrons. The light-grey points show the observed (raw) absolute flux ratios and the dark points show the *measured* absolute flux ratios as reported by MPDZ. Note that while the average stellar observation suffered an absolute flux loss of about 9%, stars centered near the middle of a pixel suffered, on average, an absolute flux loss of about 7% as compared to an absolute flux loss of about 11% for stars centered near a pixel corner. It is important to note that the vertical scatter seen in the observed flux ratios is not random but systematic; *a simple radial correction function can only partially recover the lost flux.* The measured absolute flux ratios are clustered around unity and are not a function of subpixel offset; the vertical scatter seen in the measured absolute flux ratios is random. This experiment shows that by modeling the image formation process within the detector, MPDZ was able to able fully recover all of the stellar flux lost due to the non-uniform IRAC Ch1 intrapixel quantum efficiency variations.

The vertical axis of Fig. 8 shows the observed (raw) total flux divided by the median observed total flux value of all ten thousand stars. The median values of the box-and-whisker plots (the central horizontal bar in each box) range from an excess flux of about 2% for stars centered near the center of a pixel to a flux deficit of about 2% for stars centered near the corner of a pixel. *One sees that even after the recommended flux correction (thick line of right graph of Fig. 8) is applied, an approximate **3%** peak-to-peak spread remains for many observations — this explains almost all of the **3.5%** spread seen in the right graph of Fig. 5!*

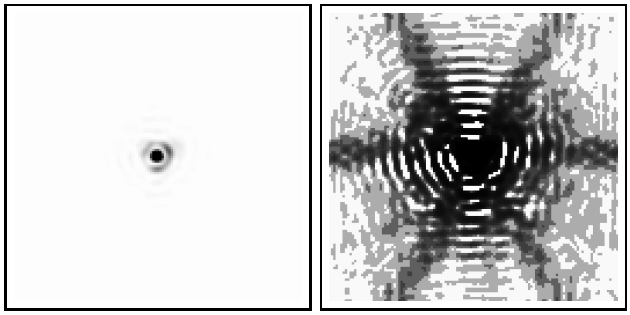

Fig. 6. A theoretical 5×5 supersampled model of the IRAC PSF for the central region of Ch1. The left (right) graph shows a linear (log) stretch; black is high and white is low. Note the the numerous weak higher-spatial-frequency features of this very complicated PSF.

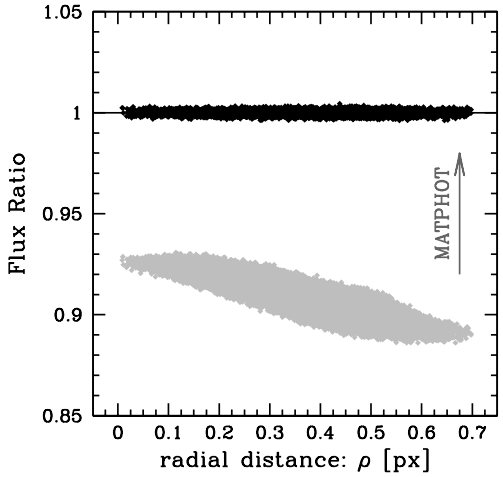

Fig. 7. MATPHOT analysis of 10,000 *simulated* IRAC Ch1 observations: observed (*lower*) versus measured (*upper*) flux ratios.

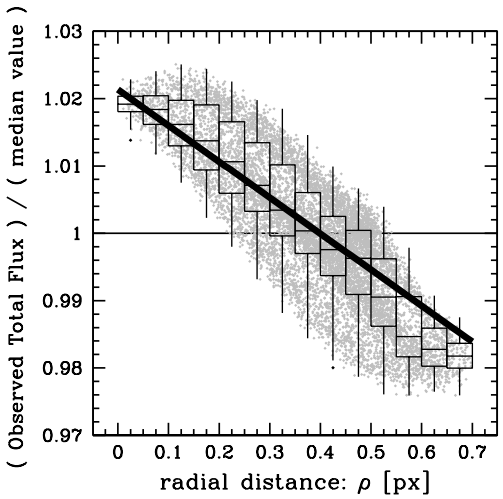

Fig. 8. MATPHOT analysis of 10,000 *simulated* IRAC Ch1 observations: *relative* observed flux ratios compared with the recommended radial flux correction (*thick line*) from the IRAC Data Handbook. Note how this figure reproduces almost exactly the observed flux loss distribution seen in Fig. 5.1 of the IRAC Data Handbook [33].

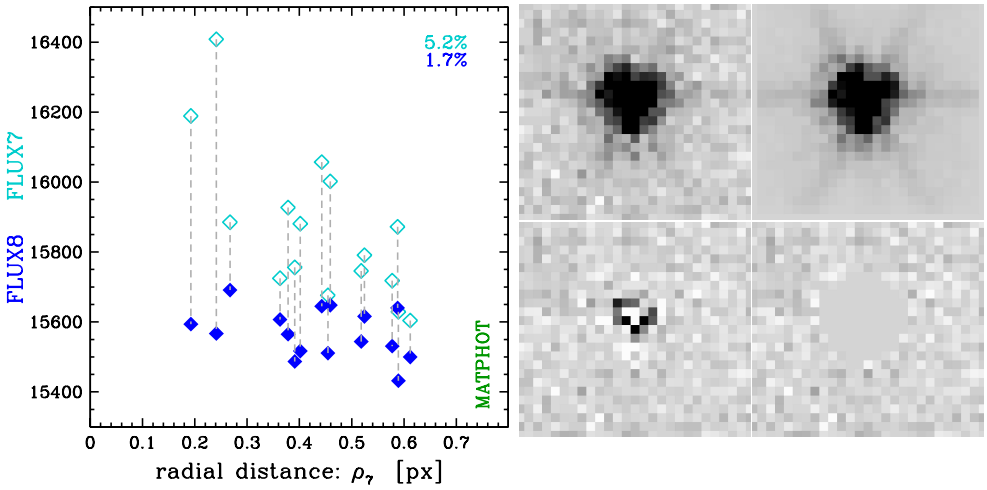

Fig. 9. MATPHOT observations of the observations shown in Fig. 1.

MATPHOT PSF-fitting photometry was performed on all of the observations using MPDZ with the theoretical 5×5 supersampled IRAC Ch1 PSF shown in Fig. 6. The open diamonds in Fig. 6 show a **5.2%** peak-to-peak spread in the raw measured stellar flux values reported by MPDZ. The upper-left image in Fig. 9 shows central portion of the first IRAC Ch1 observation. The noiseless best-fit model of the observation is shown in the upper-right image. The residuals remaining after the best-fit model is subtracted from the observation are shown in the lower-left image. The lower-right image is the same as the residual image except that all residuals within a radius of 5 pixels from the fitted center of the star have been set to zero. All of these images are displayed with the same negative linear stretch which was chosen to emphasize the faint features of the stellar image. *The filled diamonds in Fig. 9 show a **1.7%** peak-to-peak spread*; these flux values are the combination of the raw measured stellar fluxes (open diamonds) with the sum of all of residuals (positive and negative) within a radius of 5 pixels from the fitted center of the star.

MATPHOT with residuals (a.k.a. *The Lost Flux Method* [38], [39]) yields an improvement in photometric precision of more than 100% over the best results obtained with aperture photometry with the recommended radial correction: from **3.5%** peak-to-peak down to **1.7%**. Fig. 10 compares MATPHOT photometry with residuals (FLUX8: filled diamonds in Fig. 9) with the best corrected circular aperture photometry (FLUX6: filled circles in Fig. 5). The errorbars plotted with the FLUX8 values are the errors estimated by MPDZ for the raw MATPHOT flux estimates (FLUX7: open diamonds in Fig. 9).

We see that although the recorded flux of point sources was corrupted by using lossy detectors with large intrapixel quantum efficiency variations, it is possible to significantly improve the precision of stellar photometry from observations made with such detectors — if the image formation process inside the detector is accurately modeled.

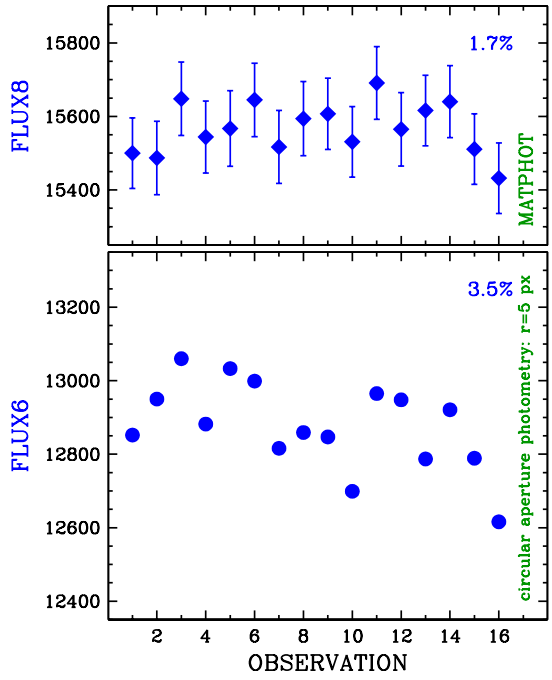

Fig. 10. MATPHOT versus circular aperture photometry.

A very interesting finding of this experiment is that even though the MATPHOT-computed Point Response Functions are not (yet) ideal matches to IRAC Ch1 stellar images, *simple aperture photometry* of stellar observations obtained with IRAC Ch1 *can be significantly improved by simply dividing the measured aperture flux by the MATPHOT-computed **volume** of the PRF* which is the convolution of the Point Spread Function and the discrete Detector Response Function. Fig. 11 compares the best *uncorrected* circular aperture photometry (FLUX5: open circles in Fig. 5) with those flux values divided by the volume of the best-fit PRF computed by MPDZ. The resultant peak-to-peak spread seen in the top graph of Fig. 11 is **1.9%**

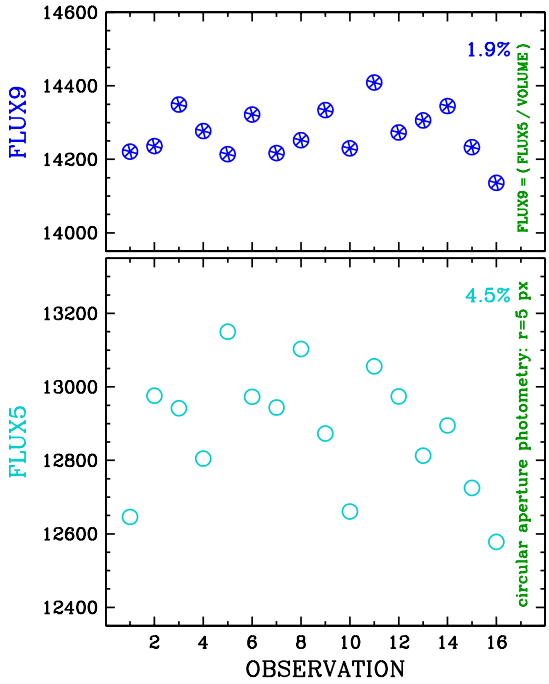

Fig. 11. Raw circular aperture fluxes corrected with MATPHOT-computed PRF volumes.

which is just slightly worse than the **1.7%** spread from the MATPHOT with residual results. This suggests that *aperture* photometry from IRAC Ch1 observations could probably be significantly improved by using a two-dimensional correction function instead of using the radial correction function currently recommended in the IRAC Data Handbook.

The derivation of that two-dimensional correction function would require a detailed analysis of a large number of dithered IRAC Ch1 unsaturated stellar observations. Fortunately, hundreds of suitable observations already exist in the *Spitzer* data archive – many which were obtained during calibration campaigns designed by the IRAC instrument team. Analyzing these observations should enable us to accurately quantify how flux loss may be a function of position within the field of view of IRAC. Comparing this external research effort with the work done by the IRAC Instrument Team should lead to a better understanding of the underlying systematics of IRAC.

VIII. Conclusion

Current near-infrared detector technology can produce space-based astronomical imagers with non-uniform pixel response functions. Large intrapixel quantum efficiency variations can cause significant loss of stellar flux depending on where a star is centered within the central pixel of an undersampled stellar image. This article showed how the precision of stellar photometry from an existing space-based near-infrared camera with a lossy detector can be significantly improved by compensating the apparent loss of stellar flux by accurately modeling the image formation process within the detector.

Much more work remains to be done. However, the possibility of significantly improving the precision and accuracy of space-based near-infrared stellar photometry appears to be excellent. Mitigating the impact of flux loss problems seen in state-of-the-art NASA-grade infrared detectors is still in its early days. Hoffmann's IRAC Ch1 intrapixel QE map [35] was the first attempt by the IRAC Instrument Team to quantify this effect. Derivation of the intrapixel QE map is an iterative process due to the apparent centroid shifting caused by the non-uniform QE variation across a pixel; given an initial estimate of the intrapixel QE map, better positions of the input stellar images can then be determined, which, in turn, enables a better measurement of the intrapixel QE map to be made. A stretch goal of 1% photometric precision might even be achievable with some *existing* space-based cameras using state-of-the-art near-infrared detector technology – if the cameras are sufficiently electronically quiet and stable.

Planning is underway for the post-cryogenic ("warm") operation of the *Spitzer Space Telescope* which will start around April 2009 after all of the liquid helium has been depleted. Only channels 1 and 2 (3.6 and 4.5 microns) of the Infrared Array Camera will be operational at full sensitivity at that time – providing an unmatched sensitivity from 3 to 5 microns until the James Webb Space telescope is launched. The other channels of all remaining instruments will not operate at the elevated temperatures (25-30K) that the spacecraft will experience during its warm mission phase.

During the past year, I have worked with IRAC Instrument Team to demonstrate that my NASA-funded MATPHOT algorithm for precision stellar photometry and astrometry using discrete Point Spread Functions can yield an improvement in the precision of bright star stellar photometry, obtained from IRAC Ch1 observations, of more than 100% over the best results obtained with aperture photometry using the recommended calibration procedures in the IRAC Data Handbook. This collaborative effort will continue with the goal of developing new calibration procedures for IRAC Ch1 and Ch2 that have the potential of significantly improving the precision of IRAC point-source photometry. This timely research effort is intended to not only enhance the science return of existing IRAC Ch1 and Ch2 observations in the Spitzer data archive but also those that will be made during the Spitzer Warm Mission.

Acknowledgment

I wish to thank W. Hoffmann, B. Glaccum, D. Elliott, P. Lowrance, and the rest of the IRAC Instrument Team for their support of this research effort. This work has been supported by grants from the National Aeronautics and Space Administration (NASA), Interagency Order Nos. NNG06EC81I, NNG05EB61I, and S-13811-G, which were awarded by the Applied Information Systems Research (AISR) Program of NASA's Science Mission Directorate.

REFERENCES

[1] T. R. Lauer, "The Photometry of Undersampled Point-Spread Functions," *Publications of the Astronomical Society of the Pacific*, vol. 111, pp. 1434–1443, Nov. 1999.

[2] R. I. Thompson, M. Rieke, G. Schneider, D. C. Hines, and M. R. Corbin, "Initial On-Orbit Performance of NICMOS," *Astrophysical Journal, Letters*, vol. 492, pp. L95–L97, Jan. 1998.

[3] Schultz, et al., *NICMOS Instrument Handbook, Version 8.0*. Baltimore: STScI, 2005.

[4] R. N. Hook and A. S. Fruchter, "Dithering, Sampling and Image Reconstruction," *ASP Conf. Ser. 216: Astronomical Data Analysis Software and Systems IX*, pp. 521–530, 2000.

[5] J. T. Trauger, et al., "The on-orbit performance of WFPC2," *Astrophysical Journal, Letters*, vol. 435, pp. L3–L6, Nov. 1994.

[6] Heyer, Biretta, et al., *WFPC2 Instrument Handbook, Version 9.0*. Baltimore: STScI, 2004.

[7] J. A. Holtzman, et al., "The performance and calibration of WFPC2 on the Huble Space Telescope," *Publications of the Astronomical Society of the Pacific*, vol. 107, pp. 156–178, Feb. 1995.

[8] J. A. Holtzman, C. J. Burrows, S. Casertano, J. J. Hester, J. T. Trauger, A. M. Watson, and G. Worthey, "The Photometric Performance and Calibration of WFPC2," *Publications of the Astronomical Society of the Pacific*, vol. 107, pp. 1065–1093, Nov. 1995.

[9] P. B. Stetson, "On the Photometric Consequences of Charge-Transfer Inefficiency in WFPC2," *Publications of the Astronomical Society of the Pacific*, vol. 110, pp. 1448–1463, Dec. 1998.

[10] A. E. Dolphin, "WFPC2 Stellar Photometry with HSTPHOT," *Publications of the Astronomical Society of the Pacific*, vol. 112, pp. 1383–1396, Oct. 2000.

[11] B. J. Pritzl, H. A. Smith, P. B. Stetson, M. Catelan, A. V. Sweigart, A. C. Layden, and R. M. Rich, "Hubble Space Telescope Snapshot Study of Variable Stars in Globular Clusters: The Inner Region of NGC 6441," *Astronomical Journal*, vol. 126, pp. 1381–1401, Sep. 2003.

[12] K. J. Mighell and I. U. Roederer, "Flickering Red Giants in the Ursa Minor Dwarf Spheroidal Galaxy: Detection of Low-Amplitude Variability in Faint Red Giant Branch Stars on 10 Minute Timescales," *Astrophysical Journal, Letters*, vol. 617, pp. L41–L44, Dec. 2004.

[13] K. J. Mighell, "Stellar photometry and astrometry with discrete point spread functions," *Monthly Notices of the Royal Astronomical Society*, vol. 361, pp. 861–878, Aug. 2005.

[14] R. A. Muller and A. Buffington, "Real-time corrction of atmspherically degraded telescope images through image sharpening," *J. Opt. Soc. Am.*, vol. 64, pp. 1200–1210, 1974.

[15] I. R. King, "The Profile of a Star Image," *Publications of the Astronomical Society of the Pacific*, vol. 83, pp. 199–201, Apr. 1971.

[16] J. L. Hora, et al., "Performance of the infrared array camera (IRAC) for SIRTF during instrument integration and test," *Proceedings of the SPIE*, vol. 4850, pp. 83–97, Mar. 2003.

[17] ——, "In-flight performance and calibration of the Infrared Array Camera (IRAC) for the Spitzer Space Telescope," *Proceedings of the SPIE*, vol. 5487, pp. 77–92, Oct. 2004.

[18] W. F. Hoffmann, J. L. Hora, J. E. Mentzell, C. Marx, and P. Eisenhardt, "Simfit and Focus Diversity: methods for determining the focus of the SIRTF telescope in space without a focus slew," *Proceedings of the SPIE*, vol. 4850, pp. 428–440, 2003.

[19] G. G. Fazio, et al., "The Infrared Array Camera (IRAC) for the Spitzer Space Telescope," *Astrophysical Journal, Supplement*, vol. 154, pp. 10–17, Sep. 2004.

[20] I. R. King, "Accuracy of measurement of star images on a pixel array," *Publications of the Astronomical Society of the Pacific*, vol. 95, pp. 163–168, Feb. 1983.

[21] N. Pogson, "Magnitudes of Thirty-six of the Minor Planets for the first day of each month of the year 1857," *Monthly Notices of the Royal Astronomical Society*, vol. 17, pp. 12–15, Nov. 1856.

[22] B. W. Kernighan and D. M. Ritchie, *The C Programming Language (2nd Edition)*. New Jersey: Prentice Hall, 1988, (ISBN: 0-131-10362-8).

[23] R. J. Hanisch, A. Farris, E. W. Greisen, W. D. Pence, B. M. Schlesinger, P. J. Teuben, R. W. Thompson, and A. Warnock, III, "Definition of the Flexible Image Transport System (FITS)," *Astronomy and Astrophysics*, vol. 376, pp. 359–380, Sep. 2001.

[24] K. J. Mighell, "The MATPHOT Algorithm for Digital Point Spread Function CCD Stellar Photometry," *ASP Conf. Ser. 281: Astronomical Data Analysis Software and Systems XI*, pp. 387–390, 2002.

[25] M. Abramowitz and I. Stegun, *Handbook of Mathematical Functions with Formulas, Graphs, and Mathematical Tables, Applied Mathematics Series, 55, eds. M. Abromowitz and I. Stegun*. Washington, D.C.: NBS, 1964.

[26] K. J. Mighell, "MATPHOT algorithm for digital point spread function CCD stellar photometry," *Proceedings of the SPIE*, vol. 4847, pp. 207–216, 2002.

[27] K. Levenberg, "A Method for the Solution of Certain Problems in Least Squares," *Quarterly of Applied Mathematics*, vol. 2, pp. 164–168, 1944.

[28] D. Marquardt, "An Algorithm for Least-Squares Estimation of Nonlinear Parameters," *SIAM Journal of Applied Mathematics*, vol. 11, pp. 431–441, 1963.

[29] K. J. Mighell, "Accurate stellar photometry in crowded fields," *Monthly Notices of the Royal Astronomical Society*, vol. 238, pp. 807–833, May 1989.

[30] ——, "Algorithms for CCD Stellar Photometry," *ASP Conf. Ser. 172: Astronomical Data Analysis Software and Systems VIII*, pp. 317–328, 1999.

[31] D. Tody, "The IRAF Data Reduction and Analysis System," *Proceedings of the SPIE*, vol. 627, pp. 733–+, 1986.

[32] ——, "IRAF in the Nineties," *ASP Conf. Ser. 52: Astronomical Data Analysis Software and Systems II*, pp. 173–183, 1993.

[33] W. T. Reach, et al., *Infrared Array Camera Data Handbook, Version 3.0 (January 20, 2006)*. Pasadena: SSC, 2006.

[34] B. Hoffmann, "25 Position Model Pixel Response Functions (PRF) Description and Quality," IRAC/TMo5-014 (Simfit Report 52 Final), 2005.

[35] ——, "Intra-pixel Variation Effect on Aperture Photometry," IRAC/TMo5-028 (Simfit Report 59; Version 2: December 10, 2005), 2005.

[36] K. J. Mighell, "Innovative image analysis software as a technology driver for advances in space telescope design," *Proceedings of the SPIE*, vol. 6265, p. 6265T, 2006.

[37] ——, "Improving the Precision of Near-Infrared Stellar Photometry by Modeling the Image Formation Process within a Lossy Detector," *Proceedings of the 2006 Advanced Mui Optical and Space Surveillance (AMOS) Technologies Conference*, pp. 201–208, 2006.

[38] ——, "The Lost Flux Method: A New Algorithm for Improving the Precision of Space-Based Near-Infrared Stellar Photometry with Lossy Detectors," *Bulletin of the American Astronomical Society*, vol. 34, p. 1132, 2006.

[39] ——, "The Lost Flux Method: A New Algorithm for Improving the Precision of Space-Based Near-Infrared Stellar Photometry with Lossy Detectors," *ASP Conf. Ser.: Astronomical Data Analysis Software and Systems XVI*, 2007, 4 pages (in press).